European Journal of Pharmacology 967 (2024) 176400

Contents lists available at ScienceDirect

European Journal of Pharmacology

journal homepage: www.elsevier.com/locate/ejphar

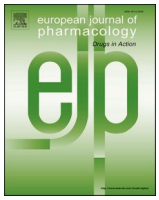

3,3′-*O*-dimethylquercetin: A bi-functional vasodilator isolated from green propolis of the Caatinga *Mimosa tenuiflora*

Ninh The Son [a,b,c], Beatrice Gianibbi [d], Alice Panti [e], Ottavia Spiga [d], Jairo Kenupp Bastos [a,**], Fabio Fusi [d,*]

[a] School of Pharmaceutical Sciences of Ribeirão Preto, Ribeirão Preto, University of São Paulo, Avenida Professor Doutor Zeferino Vaz, S/N, 14040-903, Ribeirão Preto-SP, Brazil
[b] Institute of Chemistry, Vietnam Academy of Science and Technology (VAST), 18 Hoang Quoc Viet, Caugiay, Hanoi, 10000, Vietnam
[c] Department of Chemistry, Graduate University of Science and Technology, Vietnam Academy of Science and Technology, 18 Hoang Quoc Viet, Caugiay, Hanoi, 10000, Vietnam
[d] Dipartimento di Biotecnologie, Chimica e Farmacia, Università di Siena, Via A. Moro 2, 53100, Siena, Italy
[e] Dipartimento di Scienze della Vita, Università di Siena, Via A. Moro 2, 53100, Siena, Italy

ARTICLE INFO

Keywords:
$Ca_V1.2$ channel
Flavonoid
Green propolis
$K_{Ca}1.1$ channel
Molecular modelling
Rat vascular smooth muscle

ABSTRACT

In the search for novel, bi-functional compounds acting as $Ca_V1.2$ channel blockers and K^+ channel stimulators, which represent an effective therapy for hypertension, 3,3′-*O*-dimethylquercetin was isolated for the first time from Brazilian Caatinga green propolis. Its effects were investigated through electrophysiological, functional, and computational approaches. In rat tail artery myocytes, 3,3′-*O*-dimethylquercetin blocked Ba^{2+} currents through $Ca_V1.2$ channels ($I_{Ba1.2}$) in a concentration-dependent manner, with the inhibition being reversed upon washout. The compound also shifted the voltage dependence of the steady-state inactivation curve to more negative potentials without affecting the slope of the inactivation and activation curves. Furthermore, the flavonoid stimulated $K_{Ca}1.1$ channel currents ($I_{KCa1.1}$). *In silico* simulations provided additional evidence for the binding of 3,3′-*O*-dimethylquercetin to $K_{Ca}1.1$ and $Ca_V1.2$ channels and elucidated its mechanism of action. In depolarized rat tail artery rings, the flavonoid induced a concentration-dependent relaxation. Moreover, in rat aorta rings its antispasmodic effect was inversely related to the transmembrane K^+ gradient. In conclusion, 3,3′-*O*-dimethylquercetin demonstrates effective *in vitro* vasodilatory properties, encouraging the exploration of its scaffold to develop novel derivatives for potential use in the treatment of hypertension.

1. Introduction

Propolis is a complex mixture produced by bees, consisting of resins (50%), beeswax (30%), essential oils (10%), pollens (5%), and other organic substances (5%). Its chemical composition closely mirrors that of plant buds or exudates used in its production. Among the over 300 identified chemical components of propolis, polyphenols (phenolic acids and flavonoids), terpenoids, coumarins, and prenylated derivatives are the main classes represented (Huang et al., 2014; Teixeira et al., 2005). These components can serve as indicators of its floral and geographical origin. In various regions worldwide, including the United States of America, Europe, and Japan, propolis is gaining popularity as a food supplement for improving human health and preventing diseases, as well as a valuable alternative medication (Teixeira et al., 2005). Accumulating evidence suggests that propolis exhibits analgesic, hypoglycemic (Cunha et al., 2023), antibiotic, antifungal, antiviral (Zulhendri et al., 2021), and anti-inflammatory activities (Zulhendri et al., 2022), and is cytotoxic towards tumour cells, making it a common choice in traditional medicine for treating colds, wounds, ulcers, sprains, heart failures, and diabetes (de Almeida-Junior et al., 2023).

Recent systematic review and meta-analysis studies propose that propolis supplementation could reduce oxidative stress by increasing the levels of several antioxidant enzymes, thereby potentially protecting against certain chronic diseases (Nazari-Bonab et al., 2023; Zullkiflee

Abbreviations: $I_{Ba1.2}$, Ba^{2+} current through $Ca_V1.2$ channels; $I_{KCa1.1}$, $K_{Ca}1.1$ channel current.

* Corresponding author.
** Corresponding author.
E-mail addresses: jkbastos@fcfrp.usp.br (J.K. Bastos), fabio.fusi@unisi.it (F. Fusi).

https://doi.org/10.1016/j.ejphar.2024.176400
Received 19 September 2023; Received in revised form 29 January 2024; Accepted 6 February 2024
Available online 7 February 2024

et al., 2022). Due to its high antioxidant content, propolis has been suggested as a potential antimicrobial and antioxidant food preservative, although its usage is limited by the unpleasant taste and smell (Segueni et al., 2023).

A recent review (Chavda et al., 2023), considering the main constituents of propolis, such as hesperidin, caffeic acid phenethyl ester, myricetin, quercetin, kaempferol, and limonin, used an *in silico* approach to highlight its beneficial effects against chronic diseases like tuberculosis and cancer (Altabbal et al., 2023). Remarkably, propolis extracts exhibit positive or synergistic interaction with several drugs, enhancing their pharmacological activity. This property suggests the potential use of propolis in integrative medicine to treat cancer, microbial infections, diabetes, and neurological disorders, with a low risk of altered pharmacokinetic activities (Hossain et al., 2022).

The chemical richness of propolis may contribute to cardiovascular health. A recent review (Silva et al., 2021) focused on its anti-atherosclerotic, antihypertensive, anti-haemostatic, and anti-angiogenic activities, coupled with antioxidant and anti-inflammatory properties that prevent endothelial and cardiomyocyte dysfunction. Among the varieties reviewed, Brazilian green propolis, identified by bees salivary enzymes imparting a green hue by cutting fragments of shoot apices and mixing them with wax to make propolis (Mendonça et al., 2021), exhibits the most beneficial activities. Notably, Caatinga green propolis was reported to contain many flavonoid derivatives, distinguishing it from other Brazilian propolis previously investigated (Hossain et al., 2022). However, the vasorelaxant activity of its main components is still unknown.

Vessel tone is regulated by numerous pathways, including the crucial $Ca_V1.2$ and $K_{Ca}1.1$ channels. Unravelling the component(s) responsible for the vascular activity of propolis and understanding its (their) mode of action is crucial for endorsing the nutraceutical potential of this popular natural product. The present study reports chromatographic separation, NMR-structural elucidation, and a thorough *in vitro* as well as *in silico* investigation of the vascular activity of 3,3′-*O*-dimethylquercetin isolated from green propolis of the Caatinga *Mimosa tenuiflora*. *M. tenuiflora* (Willd.) Poir., known as “jurema-preta”, is a shrubby tree of the genus *Mimosa* (family Fabaceae) naturally occurring in the northeastern Brazilian Caatinga, including the beekeeping sector (Son et al., 2022). Results demonstrate that 3,3′-*O*-dimethylquercetin is a bi-functional vasodilator capable of inhibiting vascular smooth muscle $Ca_V1.2$ channels and stimulating $K_{Ca}1.1$ channels.

2. Materials and methods

2.1. General experimental procedures

NMR spectral data (400 MHz for ^{1}H and 100 MHz for ^{13}C NMR) were acquired on a Bruker AVANCE in methanol-d_4. Column chromatography was performed with Silica gel (40–63 μm; Thermo Fisher, USA) and Sephadex LH-20 (25–100 μm; GE Healthcare, Sweden). Thin-layer chromatography (TLC) was performed on pre-coated silica gel 60 F_{254} (Merck, Germany). Visualization of TLC plates was achieved using a solution of sulfuric acid 5% in ethanol.

2.2. Propolis material

Green propolis was collected from Remanso province, Brazil, in July 2021, and taxonomically identified by Prof. Milton Groppo from the Department of Biology, University of São Paulo (Brazil). A voucher specimen, SPFR-15118, has been deposited at the Department of Biology, University of São Paulo.

2.3. Extraction and isolation

Green propolis powder (150 g) was extracted with 90% EtOH (4 x 2L x 4 h) using a Soxhlet apparatus. The resulting crude extract (38.50 g) was obtained by evaporating the combined 90% EtOH-soluble extracts under reduced pressure at 55 °C. The crude extract was then subjected to normal silica gel column chromatography [*n*-hexane-CH_3COCH_3 (1:0 to 0:1, v/v)] resulting in 13 fractions (A-M). Fraction D (5.51 g) was further separated on a normal silica gel chromatographic column [$CHCl_3$–CH_3COCH_3 (15:1 and 9:1, v/v)], to yield four fractions D41-D44. Fraction D43 (0.9 g) underwent preparative HPLC-UV [Phenomenex reverse phase column, 4 μm, 250 × 10 mm, λ_{max} 281 and 335 nm]. Elution with acetonitrile:water (6:1, v/v, 0.1% acetic acid) resulted in the isolation of 3,3′-*O*-dimethylquercetin (19.3 mg).

3,3′-*O*-Dimethylquercetin (Alday et al., 2019): yellow amorphous powder; ^{1}H-NMR (CD_3OD, 400 MHz, δ_H ppm): 7.52 (1H, dd, 2.0, 8.1 Hz, H-6′), 7.48 (1H, d, 2.0 Hz, H-2′), 6.93 (1H, d, 8.1 Hz, H-5′), 6.63 (1H, s, H-8), 6.57 (1H, s, H-6), 3.96 (3H, s, 3′-OCH_3), 3.87 (3H, s, 3-OCH_3); ^{13}C-NMR (CD_3OD, 100 MHz, δ_H ppm): 184.3 (C-4), 166.3 (C-7), 158.8 (C-5), 154.0 (C-8a), 153.2 (C-2), 152.1 (C-3′), 149.9 (C-4′), 132.9 (C-3), 123.8 (C-1′), 121.8 (C-6′), 116.8 (C-5′), 110.7 (C-2′), 103.9 (C-4a), 99.1 (C-6), 95.5 (C-8), 56.8 (3′-OCH_3), 56.8 (3-OCH_3).

2.4. Animals

All study procedures adhered strictly to the European Union Guidelines for the Care and the Use of Laboratory Animals (European Union Directive, 2010/63/EU) and received approval from the Animal Care and Ethics Committee of the University of Siena and the Italian Department of Health (7DF19.N.TBT on the 11 May 2020). Male Wistar rats (260–360 g), purchased from Charles River Italia (Calco, Italy), were housed in an animal facility with a temperature of 25 ± 1 °C and a 12:12 h dark-light cycle. They were fed with a standardised diet and had access to drinking water *ad libitum*. Animals were anaesthetized with isoflurane (4%)-O_2 gas mixture using Fluovac equipment (Harvard Apparatus, Holliston, Massachusetts, USA), followed by decapitation and exsanguination. The thoracic aorta and tail main artery were promptly isolated, placed in a modified Krebs-Henseleit solution (KHS) or an external solution, and prepared. Cells and rings were processed as detailed in sections 2.5, 2.8, and 2.9.

2.5. Cell isolation procedure for patch-clamp experiments

Smooth muscle cells were freshly isolated from the tail main artery, at 37 °C, by means of collagenase (type XI, 1.2 mg/ml) treatment in the presence of bovine serum albumin (1 mg/ml) and trypsin inhibitor (1 mg/ml) in 2 ml of 0.1 mM Ca^{2+} external solution [consisting of (in mM): 130 NaCl, 5.6 KCl, 10 HEPES, 20 glucose, 1.2 $MgCl_2$, and 5 Na-pyruvate; pH 7.4] containing 20 mM taurine. The isolation process was conducted under a gentle stream of a 95% O_2–5% CO_2 gas mixture as previously described (Carullo et al., 2020). Cells, stored in a 0.05 mM Ca^{2+} external solution containing 20 mM taurine and 0.5 mg/ml bovine serum albumin at 4 °C under normal air, were used for experiments within two days after isolation (Mugnai et al., 2014).

2.6. Ba^{2+} current through $Ca_V1.2$ channel ($I_{Ba1.2}$) recordings

The conventional whole-cell configuration of the patch-clamp technique was applied to record $I_{Ba1.2}$ from freshly isolated vascular smooth muscle cells. Borosilicate recording electrodes (WPI, Berlin, Germany) were used, having a pipette resistance of 2–4 MΩ when filled with the internal solution [containing (in mM): 100 CsCl, 10 HEPES, 11 EGTA, 1 $CaCl_2$ (pCa 8.4), 2 $MgCl_2$·6 H_2O, 5 Na-pyruvate, 5 succinic acid, 5 oxaloacetic acid, 3 Na_2-ATP, and 5 phosphocreatine; pH was adjusted to 7.4 with CsOH]. Free Ca^{2+} concentration was calculated using the computer program EqCal (BioSoft, Cambridge, UK) considering pH and Mg^{2+} concentration, as described by Fabiato & Fabiato (1979). An Axopatch 200B patch-clamp amplifier (Molecular Devices Corporation, Sunnyvale, CA, USA) was used with an ADC/DAC interface (DigiData 1200 A/B series, Molecular Devices Corporation). The setup facilitated

the generation and application of voltage pulses, recording of corresponding membrane currents, adjustment of the junction potential between the pipette and bath solution to zero, and compensation of whole-cell capacitance and series resistance (between 70 and 75%). Current signals underwent low-pass filtering at 1 kHz and were digitized at 3 kHz before being stored on the computer hard disk. Cells were continuously superfused at room temperature (20–22 °C) with an external solution containing 0.1 mM Ca^{2+} and 30 mM tetraethylammonium (TEA^+) using a peristaltic pump (LKB 2132, Bromma, Sweden), at a flow rate of 400 μl/min.

$I_{Ba1.2}$ was recorded in an external solution containing 30 mM TEA^+ and 5 mM Ba^{2+}. The current was elicited with 250-ms clamp pulses (0.067 Hz) to 10 mV from a holding potential (V_h) of either −50 mV or −80 mV. Data were collected once the current amplitude had stabilized (typically 7–10 min after achieving the whole-cell configuration). Then the various experimental protocols were performed as detailed below. Under these conditions, $I_{Ba1.2}$ remained stable for the subsequent 30–40 min (Cuong et al., 2020).

Steady-state activation curves were generated from the current-voltage relationships. Conductance (G) was calculated using the equation $G = I_{Ba1.2}/(E_m\text{-}E_{rev})$, where $I_{Ba1.2}$ is the peak current elicited by depolarizing test pulses between −50 mV and 30 mV from a V_h of −50 mV; E_m is the membrane potential; and E_{rev} is the reversal potential (estimated from the extrapolated current-voltage curves in Fig. 4). G_{max} represents the maximum Ba^{2+} conductance, calculated at potentials ≤30 mV. The G/G_{max} ratio was plotted against the membrane potential and fitted to the Boltzmann equation (Karmažínová and Lacinová, 2010).

Steady-state inactivation curves were acquired using a double-pulse protocol. After applying various conditioning potentials for 5 s, followed by a brief (5 ms) return to the V_h of −80 mV, a test pulse (250 ms) to 10 mV was delivered to evoke the current. The delay between the conditioning potential and the test pulse allowed full or near-complete deactivation of the channels, simultaneously preventing partial recovery from inactivation.

K^+ currents were blocked with 30 mM TEA^+ in the external solution and Cs^+ in the internal solution. Current values were corrected offline for leakage and residual outward currents using 10 μM nifedipine, which completely blocked $I_{Ba1.2}$.

2.7. K^+ current through $K_{Ca}1.1$ channel ($I_{KCa1.1}$) recordings

$I_{KCa1.1}$ was recorded using an external solution with the following composition (in mM): 145 NaCl, 6 KCl, 10 glucose, 10 HEPES, 5 Na-pyruvate, 1.2 $MgCl_2$, 0.1 $CaCl_2$, 0.003 nicardipine; pH 7.4]. The internal solution contained (in mM): 90 KCl, 10 NaCl, 10 HEPES, 10 EGTA, 1 $MgCl_2$, 6.41 $CaCl_2$; free Ca^{2+} concentration pCa 7.0; pH 7.4]. $I_{KCa1.1}$ was recorded for 500 ms from a V_h of −40 mV to prevent voltage-dependent K^+ channel activation. The recording stabilized in approximately 6–10 min and remained stable for at least 20–30 min (Iozzi et al., 2013). TEA^+ (1 mM), considered quite selective for $K_{Ca}1.1$ channels (Tykocki et al., 2017), was added at the end of each experiment to facilitate offline correction for leak current.

2.8. Caudal artery ring preparation and functional experiments

Endothelium-denuded rings, measuring 2 mm in width, were obtained from the tail main artery, and mounted in a homemade Plexiglas support for tension recording, following the procedures outlined in Bova et al. (1996), with minor adjustments. The endothelium was removed by gently rubbing the lumen of the rings with a thin, rough-surfaced tungsten wire. Rings were placed in a double-chambered organ bath maintained at 37 °C filled with a modified Krebs-Henseleit solution [composition (in mM): 118 NaCl, 4.75 KCl, 1.19 KH_2PO_4, 1.19 $MgSO_4$, 25 $NaHCO_3$, 11.5 glucose, 2.5 $CaCl_2$, gassed with a 95% O_2–5% CO_2 gas mixture to create a pH of 7.4]. Contractile tension was recorded using an isometric force transducer (Ugo Basile, Comerio, Italy) connected to a digital PowerLab data acquisition system (PowerLab 8/30; ADInstruments, Castle Hill, Australia) and analyzed using LabChart Pro version 7.3.7 for Windows software (ADInstruments). Initially, a preload of 2 g (1 g/mm) was applied to each ring at the start of the experiment. After a 60-min equilibration period, rings were contracted either by 90 mM KCl or 10 μM phenylephrine until reproducible responses to each stimulus were achieved. Subsequently, each ring was precontracted by 1 μM phenylephrine, and the absence of a functional endothelium was confirmed by the lack of 10 μM acetylcholine-induced relaxation.

The vasoactivity of 3,3′-*O*-dimethylquercetin was assessed on rings depolarized by either 60 mM or 90 mM KCl. Muscle tension was quantified as a percentage of the response to high KCl. High KCl concentrations were attained by directly adding KCl from a 3 M stock solution to the organ bath solution, as neither the efficacy nor potency of vasodilators is significantly affected by the resultant increase in the osmolarity compared to preparations in which the osmolarity is preserved (Magnon et al., 1998).

2.9. Aorta ring preparation and functional experiments

The thoracic aorta was gently cleaned of adipose and connective tissues and sectioned into 3-4-mm wide rings. These were mounted in organ baths between two parallel, L-shaped, stainless-steel hooks, one fixed in place and the other connected to an isometric transducer (BLPR, WPI, Berlin, Germany; Fusi et al., 2016). Rings equilibrated for 60 min in KHS under a passive tension of 1 g. Throughout this equilibration period, the solution was replaced every 15 min. Isometric tension was recorded using a digital PowerLab data acquisition system (PowerLab 8/30; ADInstruments). The viability of the rings was assessed by recording the response to 0.3 μM phenylephrine and 60 mM KCl. The endothelium was removed by gently rubbing the lumen of the ring with a forceps tip. Validation of this procedure was performed by adding 10 μM acetylcholine at the plateau of phenylephrine-induced contraction: a relaxation <15% indicated the absence of functional endothelium (Ahmed et al., 2023).

The K^+ channel opening activity of 3,3′-*O*-dimethylquercetin was examined under different conditions of high K^+-evoked depolarization (25 mM or 60 mM KCl) and compared to the activity of pinacidil (Gurney, 1994). Preparations were stimulated with two consecutive additions of 25 mM or 60 mM KCl, separated by a 45-min washout period with KHS. In the first challenge, the ring was pre-incubated for 5 min with the vehicle, while in the second it was pre-incubated for 5 min with the test drug. Responses were measured in the absence or presence of either 100 nM iberiotoxin, a specific $K_{Ca}1.1$ channel blocker or 10 μM glibenclamide, a specific $K_{ir}6$ channel blocker. Both responses were evaluated as a percentage of the response to 60 mM KCl in the functional assay.

2.10. Drugs and chemicals

The chemicals used included collagenase (type XI), trypsin inhibitor, bovine serum albumin, TEA chloride, pinacidil, phenylephrine, acetylcholine, nifedipine (Sigma Chimica, Milan, Italy), iberiotoxin (DBA Italia, Milan, Italy), and sodium nitroprusside (Riedel-De Haen AG, Seelze Hannover, Germany). All remaining substances were of analytical grade and used without additional purification. Phenylephrine was dissolved in 0.1 M HCl, while sodium nitroprusside and iberiotoxin were dissolved in distilled water. Nifedipine, directly dissolved in ethanol, and 3,3′-*O*-dimethylquercetin and pinacidil, directly dissolved in DMSO, were diluted at least 1000 times before use.

Control experiments were conducted to validate the absence of any vascular response when DMSO or ethanol was added alone at their respective final maximal concentration of 0.1% (v/v).

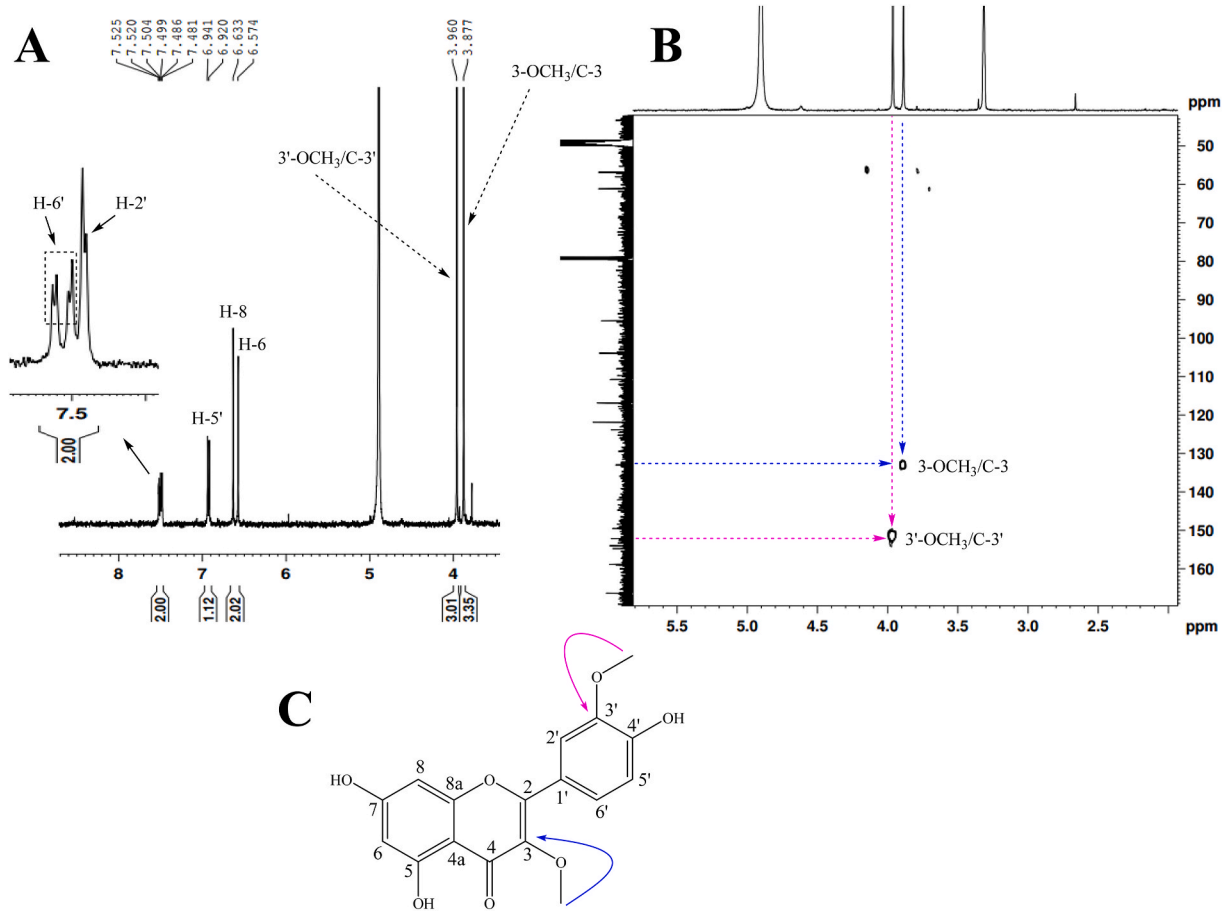

Fig. 1. 3,3′-*O*-Dimethylquercetin isolated from Brazilian Caatinga green propolis of *M. tenuiflora*. (A) The ^{1}H-NMR spectrum, (B) the key HMBC correlations, and (C) the chemical structure.

2.11. Statistical analysis

Individual values, contributing to the calculation of the group mean ± SD were derived from independent cells or rings (n). These cells or rings, although occasionally isolated from the same animal (with at least three different animals in the same group), were then randomly assigned to different treatments and assessed individually, thereby being considered as single experimental units. Data were normally distributed, and variances were not significantly different. Based on power calculation analysis (G*Power 3.1.9.4; Faul et al., 2007), a minimum of 5 rings or cells per group was deemed sufficient for a power calculation with 80% confidence.

Data analysis was conducted using pClamp 9.2.1.8 software (Molecular Devices Corporation), LabChart 7.3.7 Pro (PowerLab; ADInstruments), and GraphPad Prism version 5.04. Statistical analyses along with significance determination through repeated measures ANOVA (followed by Dunnett post-test), or Student's t-test for paired or unpaired samples (two-tailed), were performed using GraphPad Prism version 5.04. In all comparisons, $P < 0.05$ was considered significant. The pharmacological response to drugs, expressed in terms of potency (pIC_{50} value, i.e., the negative logarithm of the drug concentration causing a reduction of response equal to 50% of the maximum) and efficacy (E_{max} value, i.e., the maximum effect evoked by the drug), was obtained through nonlinear regression analysis.

2.12. 3D structure modelling

The homology model of the *Rattus norvegicus* $Ca_V1.2$ channel α_{1C} subunit was obtained as previously described (Trezza et al., 2022). Previous simulations (Carullo et al., 2022) demonstrated that the 3D Cryo-EM structure of *Homo sapiens* Ca^{2+}-bound hsSlo1-β4 channel complex (PDB ID: 6V22; Tao and MacKinnon, 2019) exhibited the highest coverage and identity with the primary structure of *Rattus norvegicus* $K_{Ca}1.1$ channel (Q62976 entry from UniProt database; Uniprot Consortium, 2023). Consequently, this structure was employed as the template for homology modelling to reconstruct the *Rattus norvegicus* $K_{Ca}1.1$ channel. The 3D coordinates of 3,3′-*O*-dimethylquercetin were retrieved from the PubChem database in sdf format (Kim et al., 2023). The compound was then prepared according to LigPrep routine from Schrödinger suites 20223, with charges assigned by Epik at pH 7.00 ± 1.00 (Greenwood et al., 2010; Schrödinger Release 2022-3, 2022; Shelley et al., 2007).

2.13. Molecular docking and molecular dynamics simulations

Molecular docking simulations were conducted using Glide protocols for standard precision and extra precision (Friesner et al., 2004, 2006; Halgren et al., 2004). In the homology model of the $Ca_V1.2$ channel, a docking pose for 3,3′-*O*-dimethylquercetin within its putative binding site was identified for subsequent classical molecular dynamics simulation. Throughout the docking process, compound input charges were retained while protein amide bond conformations were allowed to vary. The Glide flexible protocol was selected to account for a slight degree of adaptability of the receptor residues in the binding site. OH and SH groups of the side chains were allowed to rotate within a cubic box measuring 22 Å per side.

The $K_{Ca}1.1$ channel box, with dimensions of 18 Å on each side, was defined by selecting Tyr-402 as its centre. Docking boxes were generated

using the Receptor Grid Generation tool from Schrödinger suites 2022-3.

3. Subsequently, a Prime MM-GBSA simulation was performed on the $K_{Ca}1.1$ channel to minimize the protein-ligand complex. A membrane, 44.5 Å thick, was positioned at the transmembrane region, corresponding to the channel helices. Refinement of the side-chain conformations of residues within 7.00 Å from the ligand was undertaken while minimizing the complex. The OPLS4 force field was employed to parametrize the system, and solvation effects were considered by implementing VSGB as the implicit model of water (Lu et al., 2021).

The best docking pose for 3,3′-*O*-dimethylquercetin within its putative binding site in the $Ca_V1.2$ channel homology model was selected for subsequent classical molecular dynamics calculations. Before the classical molecular dynamics simulation, the $Ca_V1.2$ channel α_{1C} subunit complexed with 3,3′-*O*-dimethylquercetin docking pose was placed in a cubic water box, extending 10 Å from the protein edges, utilizing the CHARMM-GUI platform (Simplicio et al., 2014).

The N- and C-termini of the $Ca_V1.2$ channel were capped through N-acetylation and C-carbamidomethylation modifications, respectively. Histidine residues were manually protonated following visual inspection. The net charge of the system was neutralized by incorporating 16 K^+ counter-ions. In the transmembrane region of the $Ca_V1.2$ channel α_{1C} subunit, 1-palmitoyl-2-oleoyl-glycero-3-phosphocholine (POPC) entities were placed, with an 85:95 ratio between upper and lower leaflets. Finally, the CHARMM-36m force field was applied to parametrize the protein (Huang et al., 2017) and the CHARMM General Force Field was used to generate ligand parameters within the CHARMM-GUI interface. Periodic boundary conditions were maintained throughout the entire simulation, and long-range interactions were computed using Particle Mesh Ewald. Classical molecular dynamics simulation and subsequent analyses were performed on GPU using Gromacs 2022.5 (Bauer et al., 2023). Initially, system minimization was carried out with the steepest descent algorithm until convergence (forces value of 100 kJ/mol/nm) up to a maximum of 5000 steps. A cut-off radius of 1.2 nm was set for interaction calculations.

NVT equilibration of the system was achieved with the Berendsen thermostat set to 300 K after 250 ps, followed by the adoption of the NPT ensemble. Constraints on the protein backbone and lipids were gradually removed over a total of 10 ns at 1 atm pressure until convergence of the system pressure drift. The Nose-Hoover algorithm was used for temperature coupling during NPT equilibration and subsequent production simulations, while the semi-isotropic Parrinello-Rahman method was chosen for pressure coupling, known for its accuracy in membrane simulations. The low dumping parameter was set to 1 ps^{-1}.

The production run was carried out for 100 ns, utilizing a time step of 0.002 fs. Visualization of results and figure generation were performed using PyMol and Maestro user interfaces (PyMOL Molecular Graphics System, New York, NY, USA, Version 2.5, Schrödinger, LLC).

3. Results

3.1. 3,3′-O-dimethylquercetin isolation and identification

The phytochemical investigation of the 90% EtOH extract of Caatinga *M. tenuiflora* green propolis led to the isolation of a major compound. The isolated substance was obtained as a yellow amorphous powder (>95% purity). Its ^{1}H-NMR data included the singlet signals of H-6 (δ_H 6.57, 1H), H-8 (δ_H 6.63, 1H), 3′-OCH_3 (δ_H 3.96, 3H), and 3-OCH_3 (δ_H 3.87, 3H), along with signals corresponding to an ABX spin system [H-2' (δ_H 7.48, 1H, d, 2.0 Hz), H-5' (δ_H 6.93, 1H, d, 8.1 Hz), and H-6' (δ_H 7.52, 1H, dd, 2.0, 8.1 Hz)] (Fig. 1). The ^{13}C-NMR data complemented the ^{1}H-NMR data, featuring 10 quaternary carbons (δ_c 103.9–184.3), five aromatic methines (δ_c 95.5–121.8), and two methoxy groups, 3′-OCH_3 (δ_c 61.1) and 3-OCH_3 (δ_c 56.8) (see Supplementary information). The ^{1}H and ^{13}C-NMR data were further validated by the HBMC correlations, with key correlations such as H-2′ and H-6'/C-2 identifying the substitution of phenyl ring at carbon C-2. The presence of two methoxy groups at carbons C-3 and C-3′ was confirmed by the key HMBC correlations 3-OCH_3/C-3 and 3′-OCH_3/C-3′, respectively. Based on these findings and a literature survey, this isolated compound was identified as 3,3′-*O*-dimethylquercetin (Alday et al., 2019, Fig. 1).

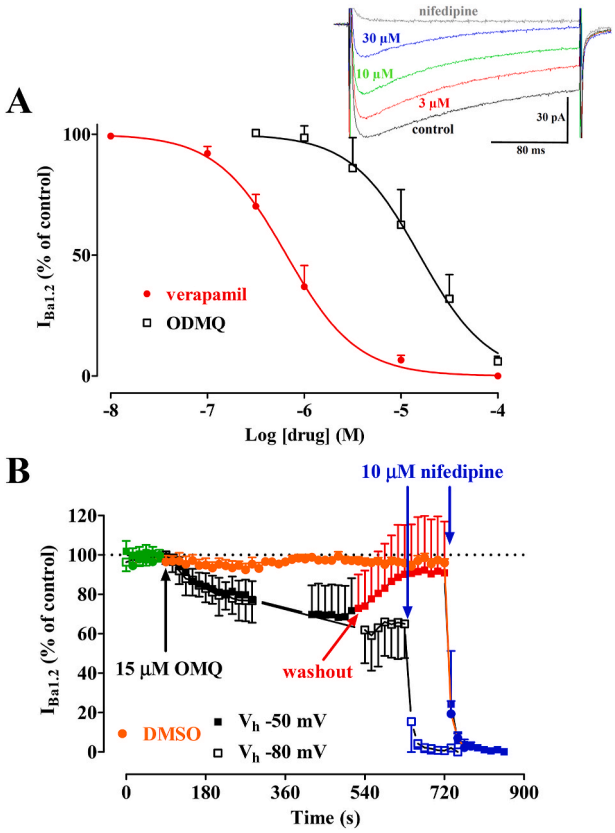

Fig. 2. 3,3′-*O*-Dimethylquercetin inhibits $I_{Ba1.2}$ in single tail artery myocytes. (A) Concentration-dependent effect of 3,3′-*O*-dimethylquercetin (ODMQ) and verapamil on $I_{Ba1.2}$. On the ordinate scale, the current amplitude is reported as a percentage of the value recorded just before the addition of the first drug concentration. Data points represent the mean ± SD (n = 4–9). Inset: traces (representative of 5 similar experiments) of $I_{Ba1.2}$, elicited with 250-ms clamp pulses to 10 mV from a V_h of −50 mV, measured in the absence (control) or presence of various concentrations of 3,3′-*O*-dimethylquercetin. The effect of 10 µM nifedipine is also shown. (B) Time course of $I_{Ba1.2}$ inhibition induced by 15 µM 3,3′-*O*-dimethylquercetin. The drug was applied at the time indicated by the arrow, and peak currents were recorded during a typical depolarization from either −50 mV or −80 mV to 10 mV, applied every 15 s (0.067 Hz) and subsequently normalized according to the current recorded just before 3,3′-*O*-dimethylquercetin addition. Drug washout gave rise to an almost complete recovery from the inhibition, while 10 µM nifedipine suppressed $I_{Ba1.2}$. The effect of vehicle (2.1 mM DMSO) is also shown. Data points are the mean ± SD (n = 6–8).

3.2. 3,3′-O-dimethylquercetin inhibited $I_{Ba1.2}$

As many flavonoids are fine regulators of $Ca_V1.2$ channels (Fusi et al., 2017), 3,3′-*O*-dimethylquercetin was investigated on $I_{Ba1.2}$, elicited by a clamp pulse to 10 mV from a V_h of −50 mV (0.067 Hz), recorded in single rat tail artery myocytes. As shown in Fig. 2A, 3,3′-*O*-dimethylquercetin caused a marked, concentration-dependent inhibition of peak $I_{Ba1.2}$ yielding a pIC_{50} value of 4.84 ± 0.20 (n = 6). Under the same experimental conditions, the Ca^{2+} antagonist verapamil exhibited a pIC_{50} value of 6.17 ± 0.12 (n = 5). The addition of 15 µM 3,3′-*O*-dimethylquercetin resulted in a time-dependent inhibition of peak $I_{Ba1.2}$, and the inhibition almost completely reversed to control values upon washout (Fig. 2B). The Ca^{2+} antagonistic activity of 3,

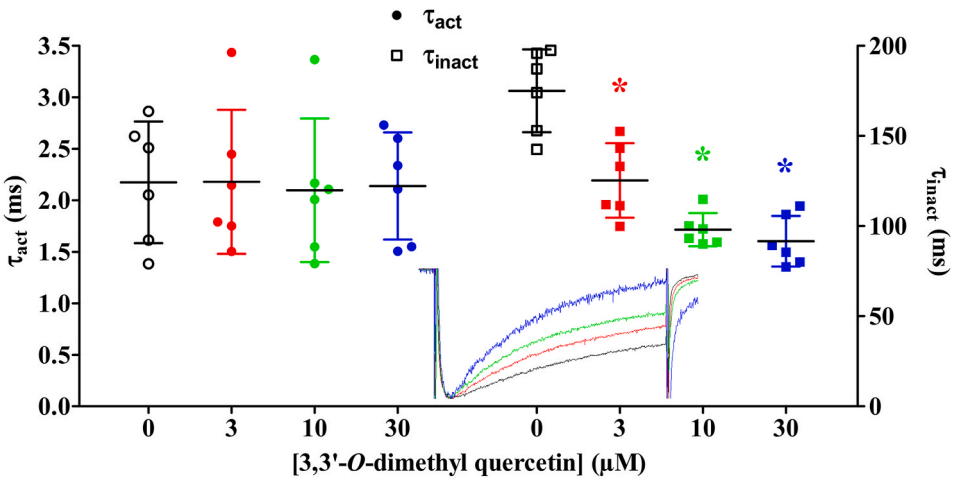

Fig. 3. 3,3′-*O*-Dimethylquercetin modifies $I_{Ba1.2}$ kinetics of single tail artery myocytes. Time constants for activation (τ_{act}) and inactivation (τ_{inact}) were measured in the absence or presence of various concentrations of 3,3′-*O*-dimethylquercetin. Lines and bars represent the mean ± SD (n = 6). *P < 0.05 vs. control (0), repeated measures ANOVA and Dunnett post-test. Inset: current recordings, taken from Fig. 2A inset, are sized so that the peak amplitude of the traces in the presence of the drug matched that of the control.

3′-*O*-dimethylquercetin did not change when V_h was shifted from −50 mV to −80 mV (Fig. 2B).

The time course of $I_{Ba1.2}$ activation and inactivation were described by a mono-exponential function. 3,3′-*O*-Dimethylquercetin did not affect the τ of activation but significantly accelerated the τ of inactivation (Fig. 3).

Fig. 4A shows the effect of 3,3′-*O*-dimethylquercetin on the current-voltage relationship recorded from a V_h of −50 mV. Neither the apparent maximum (15 mV) nor the threshold (−40 mV) of the current-voltage relationship was altered by the presence of 15 μM 3,3′-*O*-dimethylquercetin. However, the compound significantly reduced $I_{Ba1.2}$ in the range of membrane potential values from −20 mV to 10 mV.

The voltage dependence of 3,3′-*O*-dimethylquercetin inhibition of $I_{Ba1.2}$ was further explored by analysing the steady-state activation curves, derived from the current-voltage relationships shown in Fig. 4A and fitted with the Boltzmann equation. The 50% activation potential (0.43 ± 3.93 mV, control, 1.44 ± 4.32 mV, 15 μM 3,3′-*O*-dimethylquercetin, and 1.37 ± 3.54 mV, washout; P = 0.0515) and the slope factor (7.19 ± 0.22 mV, 6.82 ± 0.64 mV, and 7.26 ± 0.31 mV, respectively; P = 0.1316) of the activation curve remained unaffected (Fig. 4B). In contrast, 3,3′-*O*-dimethylquercetin, significantly shifted the steady-state inactivation curve (i.e., channel availability) toward more hyperpolarizing potentials (Fig. 4B). The 50% inactivation potential changed from −22.86 ± 4.86 mV (n = 6, control) to −29.62 ± 4.44 mV (15 μM 3,3′-*O*-dimethylquercetin; P = 0.0010). However, the slope factor was not affected by the flavonoid (−9.47 ± 4.03 mV and −8.48 ± 1.89 mV, respectively; P = 0.4549). The shift in the inactivation curve induced by 15 μM 3,3′-*O*-dimethylquercetin resulted in a marked reduction of the Ba^{2+} window current. At 0 mV, for example, the relative amplitude decreased to 0.03 compared to the relative amplitude of 0.11 observed under control conditions.

3.3. 3,3′-O-dimethylquercetin stimulated $I_{KCa1.1}$

Given that many flavonoids are recognized as effective $K_{Ca}1.1$ channel stimulators (Fusi et al., 2020), the effect of 3,3′-*O*-dimethylquercetin on iberiotoxin-sensitive $I_{KCa1.1}$ was investigated (Saponara et al., 2006). The addition of 30 μM 3,3′-*O*-dimethylquercetin caused a significant stimulation of the current amplitude within the membrane potential range of 20–70 mV (Fig. 5): current stimulation reached a plateau in about 3 min.

3.4. 3,3′-O-dimethylquercetin relaxed caudal artery rings stimulated by KCl

This series of experiments was performed to assess whether the Ca^{2+} antagonistic activity of 3,3′-*O*-dimethylquercetin translates to a vasodilatory effect in the intact vascular tissue. Caudal artery rings were depolarized by either a submaximal (60 mM) or a maximal (90 mM) concentration of KCl. In rings pre-incubated with cumulative concentrations of 3,3′-*O*-dimethylquercetin, the subsequent response to 90 mM KCl gradually diminished (Fig. 6A), yielding a pIC_{50} value of 4.39 ± 0.22 (n = 5; Fig. 6B). Under the same experimental conditions, the Ca^{2+} antagonist verapamil showed a pIC_{50} value of 6.20 ± 0.31 (n = 5). Furthermore, in rings pre-contracted by 60 mM KCl, 3,3′-*O*-dimethylquercetin induced a concentration-dependent relaxation with a pIC_{50} value of 5.47 ± 0.78 (n = 5; P = 0.0179 vs. 90 mM KCl), while that of verapamil was 6.93 ± 0.37 (n = 6; P = 0.0067).

Finally, the antispasmodic effect of 3,3′-*O*-dimethylquercetin reversed to control values upon washout in about 1 h (Fig. 6C).

3.5. Antispasmodic activity of 3,3′-O-dimethylquercetin and pinacidil in aorta rings stimulated by KCl

K^+ channel opening activity was assessed in aorta rings stimulated by 25 mM or 60 mM KCl, in the presence of either vehicle or tested compounds. As shown in Fig. 7 30 μM 3,3′-*O*-dimethylquercetin significantly antagonised both 25 mM KCl- and 60 mM KCl-induced contractions, though with different efficacy (44.4 ± 19.2% and 13.8 ± 10.3%, n = 5; P = 0.0137). Similar results were observed with pinacidil (97.7 ± 3.3% and 19.6 ± 8.4%, n = 5; P < 0.0001).

Iberiotoxin (100 nM) reduced the antispasmodic activity of 3,3′-*O*-dimethylquercetin (P = 0.2436), while glibenclamide (10 μM) that of pinacidil by about 50% (P = 0.0009; Fig. 7).

3.6. 3,3′-O-dimethylquercetin-$Ca_V1.2$ channel complex acquired stable interactions during classical molecular dynamics simulation

The molecular docking simulation of 3,3′-*O*-dimethylquercetin within the homology model of the *Rattus norvegicus* $Ca_V1.2$ channel resulted in a binding affinity of −9.408 kcal/mol (XP GScore) and showed hydrophobic interactions with multiple residues within the binding pocket, which is commonly occupied by well-known channel blockers (Zhao et al., 2019, Fig. 8). Specifically, the 3′-OCH_3 and 4′-OH groups of the B ring formed hydrophobic interactions with Ile-1180,

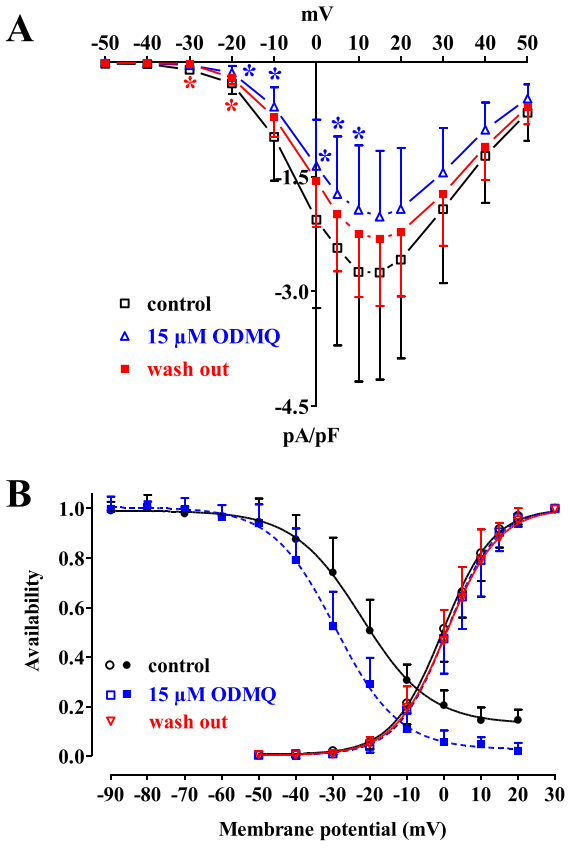

Fig. 4. Voltage dependency of 3,3′-*O*-dimethylquercetin-induced inhibition of $I_{Ba1.2}$ in single tail artery myocytes. (A) Current-voltage relationships, recorded from a V_h of −50 mV, constructed before the addition (control), in the presence of 15 μM 3,3′-*O*-dimethylquercetin (ODMQ), and after drug washout. Data points are the mean ± SD (n = 6). *P < 0.05 vs. control, repeated measures ANOVA and Dunnett post-test. (B) The effect of 3,3′-*O*-dimethylquercetin on the voltage dependence of $Ca_V1.2$ channel activation and inactivation. Steady-state inactivation curves in the absence (control) or presence of 15 μM 3,3′-*O*-dimethylquercetin were fitted to the Boltzmann equation. Peak current values were used. The current measured during the test pulse was plotted against the membrane potential and is expressed as availability. Steady-state activation curves were obtained from the current-voltage relationships in panel A and fitted to the Boltzmann equation. Data points are the mean ± SD (n = 6).

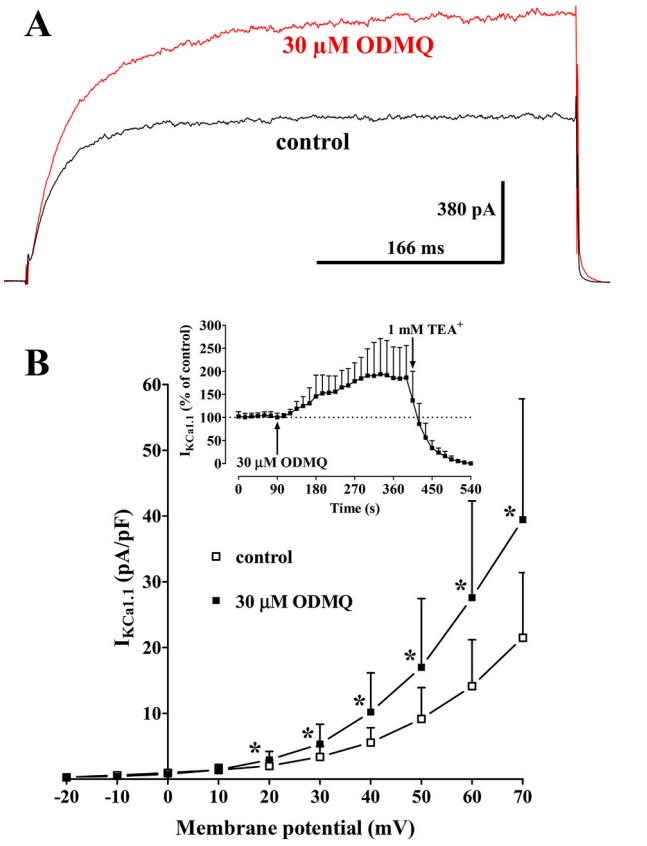

Fig. 5. 3,3′-*O*-Dimethylquercetin stimulates $I_{KCa1.1}$ in single tail artery myocytes. (A) Original recordings (average traces of 7 cells) of conventional whole-cell $I_{KCa1.1}$ elicited with a 500-ms voltage step from a V_h of −40 mV to 70 mV, measured in the absence (control) and presence of 30 μM 3,3′-*O*-dimethylquercetin (ODMQ). (B) Current-voltage relationships obtained before the addition (control) and in the presence of 30 μM 3,3′-*O*-dimethylquercetin (ODMQ). On the ordinate scale, the response is reported as current density in pA/pF. Data points are the mean ± SD (n = 7). *P < 0.05 vs. control, Student's *t*-test for paired samples. Inset: Time course of $I_{KCa1.1}$ stimulation induced by 30 μM 3,3′-*O*-dimethylquercetin. The drug was applied at the time indicated by the arrow, and peak currents were recorded during a typical depolarization from −40 mV to 70 mV, applied every 15 s (0.067 Hz) and subsequently normalized according to the current recorded just before 3,3′-*O*-dimethylquercetin addition. Tetraethylammonium (TEA^+; 1 mM) addition suppressed $I_{KCa1.1}$. Data points are the mean ± SD (n = 7).

Ile-1181, Ala-1183, Phe-1184, and Leu-777. The core of the molecule engaged in non-polar interactions with the hydrophobic residues Phe-1143, Phe-778, Phe-730, and Leu-733. Notably, the only polar amino acid of the network, Thr-734, was not directly involved in hydrogen bond interactions. Additionally, longer-range and less contributing hydrophobic interactions were observed with Leu-685, Leu-688, and Leu-678 residues, which are in proximity to the binding site (Fig. 8).

Molecular dynamics simulation of the protein-ligand complex showed that 3,3′-*O*-dimethylquercetin root mean square deviation of coordinates (RMSD) from the starting ligand pose within the $Ca_V1.2$ channel putative binding site was consistently low, ranging from 0.15 to 0.2 nm (Fig. 9). This indicates stability and reliability of the initial prediction. The structural integrity of the $Ca_V1.2$ channel α_{1C} subunit was further confirmed by superimposing the protein backbone RMSD trends of the channel in complex with the ligand and in the free state (Fig. 9). This stability was also supported by the radius of gyration calculations, revealing mean values of 2.19 ± 0.01 nm and 2.22 ± 0.02 nm for the protein-ligand complex and the free state, respectively. During classical molecular dynamics simulation, the ligand consistently formed stable interactions with polar residues within the binding pocket and oriented its aromatic core and B ring to engage in π-π stacking interactions with Phe-778 and Phe-1143, while maintaining previously reported hydrophobic interactions with Phe-778 and Asn-771 (corresponding to Phe-656 and Asn-649 of the rabbit $Ca_V1.1$ channel). Notably, the 4′-OH group acted as both a hydrogen-bond donor and acceptor, interacting simultaneously with the Thr-734 backbone and Asn-771 side chain (Fig. 10). The overall non-bonded interaction energy between the $Ca_V1.2$ channel and 3,3′-*O*-dimethylquercetin during the classical molecular dynamics simulation yielded a value of −145.2 ± 6.3 kJ/mol (−34.7 ± 1.5 kcal/mol).

3.7. 3,3′-O-dimethylquercetin interaction network with the $K_{Ca}1.1$ channel

3,3′-*O*-Dimethylquercetin formed a tight interaction network within the putative binding pocket located inside the $K_{Ca}1.1$ channel, primarily characterized by π-π stacking interactions with Phe-461, Tyr-398, and Tyr-402 involving both the core of the molecule and the B ring (Fig. 11). The 4′-OH group established a hydrogen bond with the backbone of Gly-

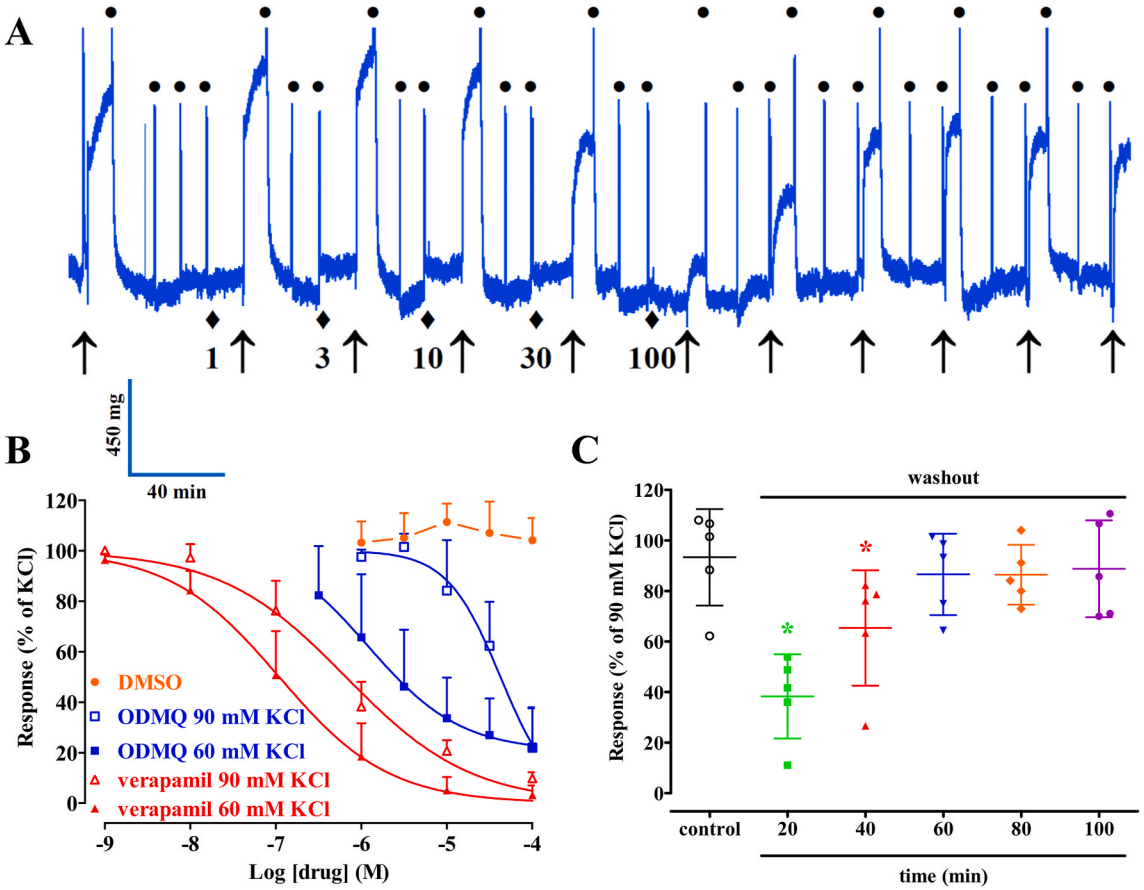

Fig. 6. 3,3′-*O*-Dimethylquercetin inhibits high KCl-induced contraction of caudal artery rings. (A) Trace (representative of 4 similar experiments) of the antispasmodic activity of cumulative concentrations of 3,3′-*O*-dimethylquercetin (diamonds with numbers; μM) pre-incubated for 10 min before the addition of 90 mM KCl (arrows) and its reversibility by washout (dots). (B) Concentration-response curves for 3,3′-*O*-dimethylquercetin and verapamil in rings challenged by either 60 mM or 90 mM KCl. In the ordinate scale, relaxation is reported as a percentage of the initial tension induced by 60 mM KCl or 90 mM KCl in the ring functional test, respectively. The effect of vehicle (0.14, 0.42, 1.41, 4.23, and 14.08 mM DMSO) is also shown. Data points represent the mean ± SD (n = 4–6). (C) Washout of the antispasmodic effect of 3,3′-*O*-dimethylquercetin. Points represent the response to 90 mM KCl recorded in the ring functional test (control) and during the washout of 100 μM 3,3′-*O*-dimethylquercetin. Lines and bars represent the mean ± SD (n = 5). *P < 0.05 vs. control, repeated measures ANOVA and Dunnett post-test.

399, while the 7-OH group interacted with Val-464, resulting in a docking score of −6.913 kcal/mol. Following the MM-GBSA minimization of the protein-ligand complex, additional interactions involving Lys-458 and Hie-460 (His-460 in ε tautomeric state) were detected (with the previous ones remaining unaffected), leading to an overall free Gibbs energy of binding (ΔG) of −61.60 kcal/mol (Fig. 11).

4. Discussion

The main findings of the present study highlight that 3,3′-*O*-dimethylquercetin is an effective and bi-functional *in vitro* vasodilator, as supported by both electrophysiological and functional evidence. Although this flavonoid has been previously identified in various natural sources, such as Mexican *Populus fremontii* propolis (Alday et al., 2019) and Australian sunflower honey (Yao et al., 2004), the present study marks the first identification of 3,3′-*O*-dimethylquercetin in Brazilian green propolis and its isolation from the *Mimosa* genus. Consequently, the compound could serve as a chemotaxonomic marker for *Mimosa* green propolis.

The current investigation provides the first direct experimental evidence establishing 3,3′-*O*-dimethylquercetin as a blocker of vascular $Ca_V1.2$ channels. The supportive evidence for this conclusion is as follows: 1) in single vascular myocytes, 3,3′-*O*-dimethylquercetin inhibited $I_{Ba1.2}$ in a concentration-dependent manner; 2) this inhibition was likely attributed to direct interaction with the channel protein; 3) 3,3′-*O*-dimethylquercetin stabilized the $Ca_V1.2$ channel in its inactivated state; and 4) due to its relaxation of vascular smooth muscle contraction resulting from the opening of $Ca_V1.2$ channels, the $I_{Ba1.2}$ blockade is presumed to have functional relevance complementing previous data obtained both *in vivo* in spontaneously hypertensive rats and *in vitro* in vascular preparations (Kubota et al., 2004; Maruyama et al., 2009) where a similar mechanism of action was hypothesized to underlie the relaxant effects of propolis.

The inhibition of $I_{Ba1.2}$ induced by 3,3′-*O*-dimethylquercetin at a frequency of 0.067 Hz, allowing full recovery between pulses from $Ca_V1.2$ channel inactivation in rat tail artery myocytes (Saponara et al., 2002), is tonic and developed independently of channel activation (Kuriyama et al., 1995). This suggests a selective inhibition of the resting channel state. Additionally, like nicardipine (Bean, 1984), 3,3′-*O*-dimethylquercetin shifted the channel availability towards more hyperpolarizing potentials, commonly interpreted as a consequence of high-affinity drug binding and stabilization of inactivated channels (Bean, 1984). Interestingly, $Ca_V1.2$ channel blockade exhibited by 3,3′-*O*-dimethylquercetin was not voltage-dependent, as comparable current inhibition was observed at V_h values of both −50 mV and −80 mV. The stabilization of the inactivated state occurred rapidly, affecting $I_{Ba1.2}$ inactivation during the 250 ms-long depolarizing step. Notably, this effect was observed under experimental conditions limiting or even abolishing Ca^{2+}-dependent inactivation of the channel (using Ba^{2+} as a charge carrier instead of Ca^{2+} and clamping intracellular Ca^{2+} at 4 nM

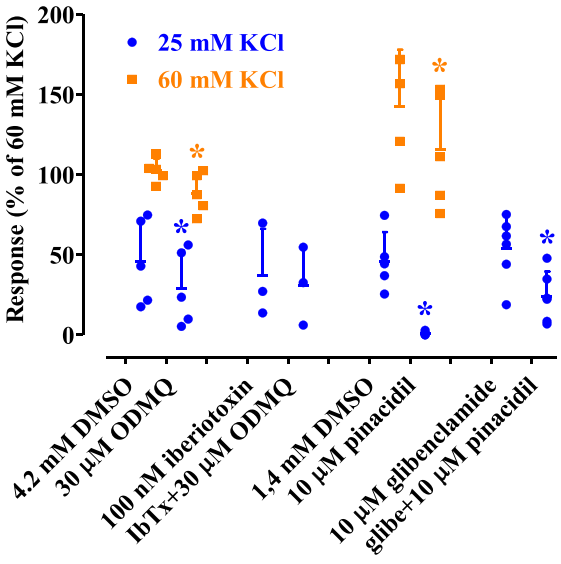

Fig. 7. 3,3′-*O*-Dimethylquercetin and pinacidil inhibit high KCl-induced contraction of aorta rings. Rings, pre-incubated for 5 min with DMSO, were stimulated by either 25 mM or 60 mM KCl for 15 min and then washed in KHS for 45 min. Pinacidil (10 µM) or 3,3′-*O*-dimethylquercetin (30 µM) were added 5 min before the second challenge by KCl. The effects of 100 nM iberiotoxin and 10 µM glibenclamide are also shown. In the ordinate scale, response is reported as a percentage of the tension induced by 60 mM KCl in the ring functional test. Lines and bars represent mean ± SD (n = 3–6). *P < 0.05 vs DMSO, Student's *t*-test for paired samples.

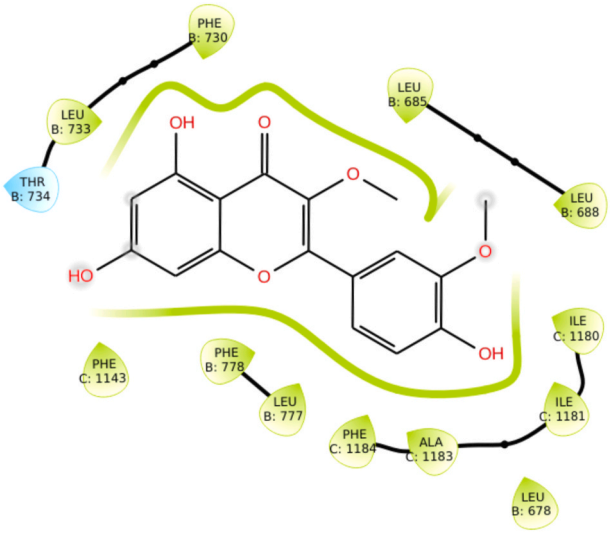

Fig. 8. Best binding pose of 3,3′-*O*-dimethylquercetin within the $Ca_V1.2$ channel α_{1C} subunit following molecular docking simulation. Hydrophobic interactions between the ligand and residues within 4.00 Å of 3,3′-*O*-dimethylquercetin are shown. The colouring of residues follows a polar (cyan) and non-polar (green) scheme. The numbering of interacting residues with their corresponding chain id are depicted for clarity.(For interpretation of the references to colour in this figure legend, the reader is referred to the Web version of this article.)

with EGTA to prevent smooth muscle cell contraction during recordings), This evidence suggests a direct interaction of the flavonoid with the inactivation machinery of the channel, though single-channel experiments are required to confirm or refute this hypothesis. Taken together, within the context of the "state-dependent pharmacology" of the channel, three simultaneous mechanisms operated by 3,3′-*O*-dimethylquercetin contribute to $Ca_V1.2$ channel block: state-independent (tonic), state-dependent open channel inhibition (faster $Ca_V1.2$ channel inactivation kinetics as observed with dihydropyridine and phenylalkylamine $Ca_V1.2$ channel blockers; McDonald et al., 1994), and state-dependent inactivated channel stabilization. The complete reversibility of 3,3′-*O*-dimethylquercetin $I_{Ba1.2}$ antagonism observed in this study suggests a relatively weak interaction of the drug with the channel protein.

The leftward shift in the steady-state inactivation curve induced by 3,3′-*O*-dimethylquercetin resulted in a marked reduction of the window current. This current is considered physiologically relevant as it is believed to play a crucial role in both the generation and regulation of vascular smooth muscle tone (Fransen et al., 2012). Hence, this property could contribute to the observed vasodilatory effect of the flavonoid previously documented *in vivo* (Kubota et al., 2004; Maruyama et al., 2009). Conversely, neither the slope nor the 50% activation potential of the steady-state activation curve was affected by 3,3′-*O*-dimethylquercetin. This indicates that the sensitivity of the channel activation mechanism to the membrane voltage remained unaltered.

In silico simulations have provided valuable insights into the molecular mechanism underlying the blockade of $Ca_V1.2$ channels by 3,3′-*O*-dimethylquercetin. Interestingly, the flavonoid was predicted to bind to a pocket where well-known Ca^{2+} antagonists also bind (Zhao et al., 2019). The simulations indicated excellent affinity (−9.408 kcal/mol after molecular docking), stability within the cavity after classical molecular dynamic simulation (ligand RMSD being 0.15–2 nm), and the ability to interact with Phe-778 and Phe-1143, key residues for drug pharmacological activity. Moreover, the interaction with Phe-1143 must be crucial for the inhibitory activity of the flavonoid, as mutagenesis experiments demonstrated the importance of this residue for channel pore formation. However, Ser-1141, which participates in the interaction network of dihydropyridines such as Bay K 8644 and nifedipine (Zhao et al., 2019), was not involved in the binding of the flavonoid. Collectively, this evidence suggests that the conformational change of the α_{1C} subunit likely occurring upon binding of 3,3′-*O*-dimethylquercetin could lead to a structural reorganization of the entire $Ca_V1.2$ channel, thereby explaining the blockade of the current. Nonetheless, future mutagenesis experiments are necessary to confirm or refute such a hypothesis.

The computational approach has yielded promising results in elucidating the mechanism of 3,3′-*O*-dimethylquercetin binding to *Rattus norvegicus* $Ca_V1.2$ channels. A direct comparison with ground truth data, represented by co-crystals with verapamil or nifedipine (−6.735 and −4.563 kcal/mol docking scores of the co-crystallized poses, respectively, starting from 6JPA and 6JPC Cryo-EM models of the protein data bank; Zhao et al., 2019) was feasible. While the analysis focused on the well-known and characterized α_{1C} subunit, which contains a total of 2169 residues, it is important to note that $Ca_V1.2$ channels consist of several additional subunits. Therefore, future studies will be necessary to further characterize the binding site(s) in more detail and to unequivocally determine the mode of action of 3,3′-*O*-dimethylquercetin.

The conventional whole-cell method used in this study involves the dialysis of the cytoplasm. Consequently, it is reasonable to hypothesise that the inhibition of $I_{Ba1.2}$ by 3,3′-*O*-dimethylquercetin is linked to a direct interaction of the drug with the channel protein, as indicated by the *in silico* analysis. However, it is worth noting that the potential involvement of intracellular signalling pathways that survive dialysis cannot be ruled out.

In addition to its $Ca_V1.2$ channel-blocking activity, 3,3′-*O*-dimethylquercetin induced a significant increase in current amplitude through the $K_{Ca}1.1$ channel, aligning with the vasorelaxant behaviour observed in the intact tissue (see below). $I_{KCa1.1}$ was characterized by using the channel blocker TEA^+ which, at 1 mM concentration, is considered relatively selective for $K_{Ca}1.1$ channels (Tykocki et al.,

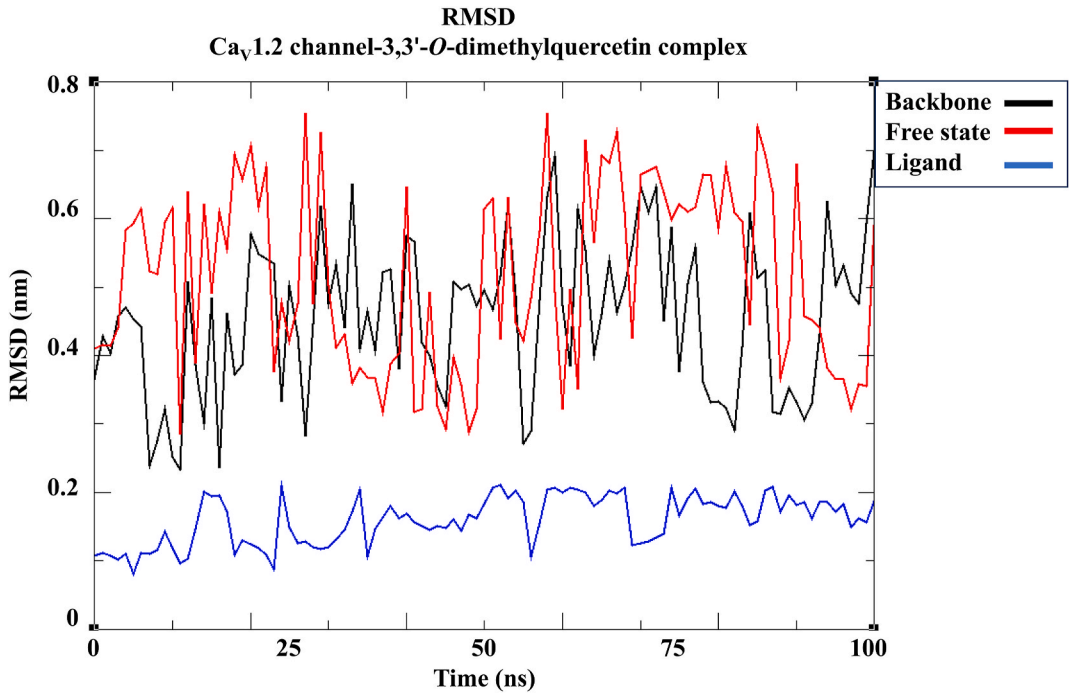

Fig. 9. Root mean square deviation trends of Ca$_V$1.2 channel-3,3′-*O*-dimethylquercetin complex during classical molecular dynamics simulation. The computed root mean square deviation (RMSD) during the whole molecular dynamics simulation showed stability of both the protein backbone (black line) and the ligand pose (blue line). Time and RMSD are represented in the X- and Y-axis, respectively. For comparison, the protein backbone trend for the channel-free state is also reported (red line).(For interpretation of the references to colour in this figure legend, the reader is referred to the Web version of this article.)

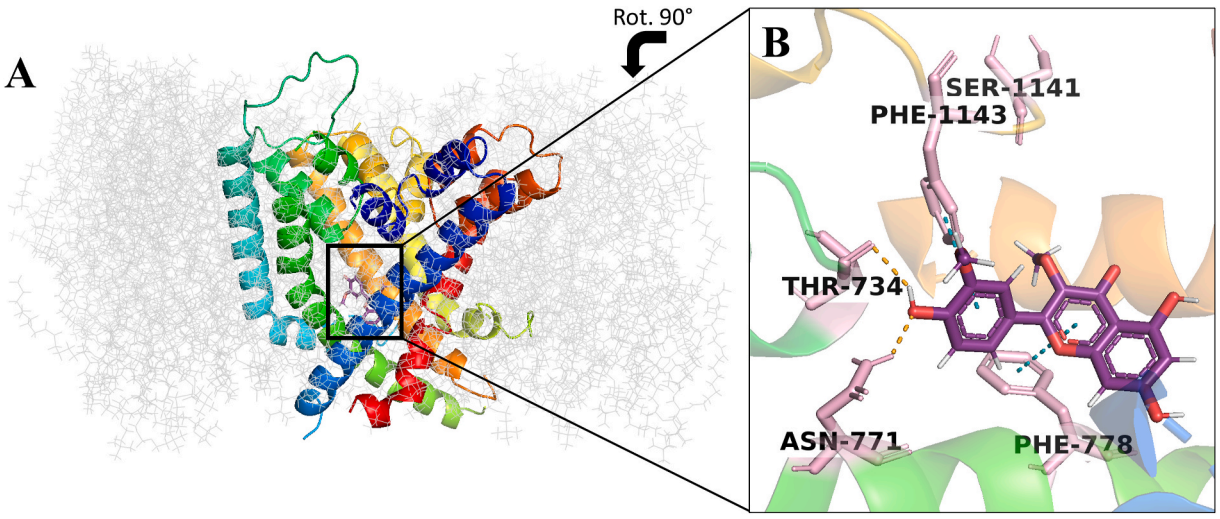

Fig. 10. Ca$_V$1.2 channel α_{1C} subunit in complex with 3,3′-*O*-dimethylquercetin after molecular dynamics simulation. (A) Protein-ligand complex. Lipids are reported as grey lines and protein backbone as cartoon-like representations in chain-based colouring schemes. The ligand (purple ball-and-sticks) is positioned near the centre of the channel subunit pore. (B) Enlarged view of the most representative binding pose of 3,3′-*O*-dimethylquercetin following the reorientation of the B ring during classical molecular dynamics simulation. Hydrogen bonds (light orange dashed lines) and π-π stacking interactions (blue dashed lines) formed by the ligand with residues of the binding pocket (pink ball-and-sticks) are shown. The colour scheme of the protein backbone is the same as in panel A. Ser-1141, not interacting with the ligand, is reported only as a reference residue.(For interpretation of the references to colour in this figure legend, the reader is referred to the Web version of this article.)

2017). It's important to note that TEA^+ also potently blocks $K_V1.1$, $K_V1.2$, and $K_V3.1$ channels. However, it should be emphasized that $K_V1.1$ and $K_V3.1$ channels are not expressed in rat tail artery myocytes (Xu et al., 2000) and the V_h of −40 mV used for $I_{KCa1.1}$ recordings should have limited or even avoided the contribution of $K_V1.2$ channels to the overall current amplitude.

The marked binding affinity (−6.913 kcal/mol) obtained in the computational simulations strongly supported the $K_{Ca}1.1$ channel stimulation induced by 3,3′-*O*-dimethylquercetin. Mutagenesis experiments have suggested that the receptor S6/RCK linker might be responsible for both modulator binding to and activation of the $K_{Ca}1.1$ channel (Gessner et al., 2012). Specifically, Tyr-402 is crucial for channel activation and for coupling with downstream effectors. *In silico* simulations demonstrated that 3,3′-*O*-dimethylquercetin established a tight interaction network with residues in a putative binding pocket close to the linker region, supporting the electrophysiology evidence and

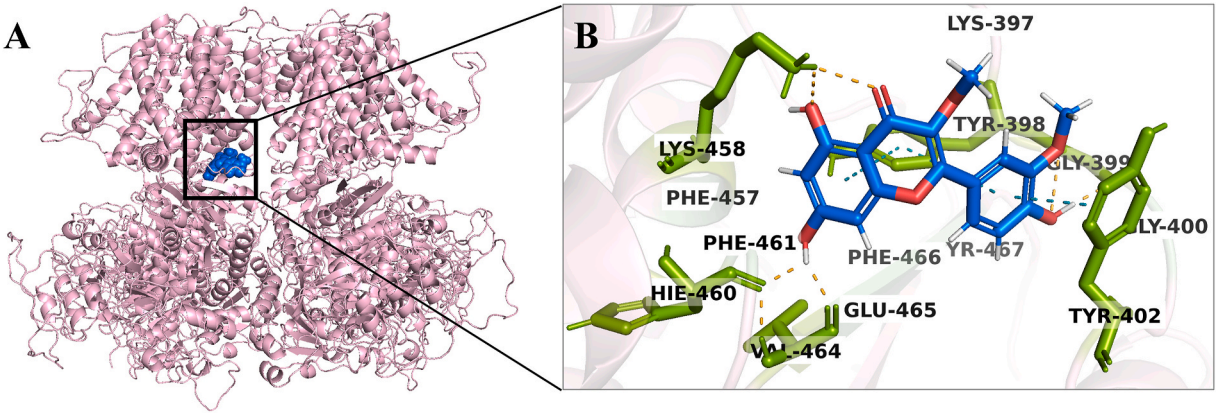

Fig. 11. $K_{Ca}1.1$ channel in complex with 3,3′-*O*-dimethylquercetin obtained with MM-GBSA simulation. (A) Protein-ligand complex. The $K_{Ca}1.1$ channel is represented as a pink cartoon-like structure and the investigated binding pocket as blue spheres. (B) Enlarged view of the 3,3′-*O*-dimethylquercetin (blue ball-and-stick) interaction network with surrounding residues (green ball-and-sticks). Hydrogen bonds are represented as light orange dashed lines, π-π stacking interactions as blue dashed lines. For clarity, only interacting residues forming polar contacts are shown in green, while all interacting residues of the cavity are labelled in black.(For interpretation of the references to colour in this figure legend, the reader is referred to the Web version of this article.)

providing insightful details about its molecular mechanism. Unfortunately, the resolution of the intra-cytoplasmic region in classical molecular dynamics simulation did not permit further investigation of the binding mode inside the $K_{Ca}1.1$ channel. Nevertheless, the Gibbs free energy of binding after minimization of the protein-ligand complex yielded promising results (−61.60 kcal/mol). It's important to note that the lack of any experimentally ascertained complex involving a $K_{Ca}1.1$ channel and a stimulator limited the present study to a putative binding site based on mutagenesis experiments. While 3,3′-*O*-dimethylquercetin could potentially have a good affinity profile for other channel regions, additional resources are needed to correlate the resulting affinity with a biological function.

The inhibition of the $Ca_V1.2$ channel by 3,3′-*O*-dimethylquercetin was also observed in intact tissues under conditions of full membrane depolarization, specifically in tail artery rings stimulated by either 60 mM or 90 mM KCl concentrations. Under conditions mimicking those used in the patch-clamp experiments to evoke $I_{Ba1.2}$, 3,3′-*O*-dimethylquercetin caused relaxation, and its potency and efficacy were consistent with those calculated in the electrophysiology experiments. Furthermore, the myorelaxant effect of the drug was completely reversed by washout, like what was observed in the patch-clamp experiments. The flavonoid exhibited both antispasmodic and spasmolytic activities. Additionally, the observation that the antispasmodic activity of 3,3′-*O*-dimethylquercetin was directly correlated with the transmembrane chemical gradient for K^+ (Gurney, 1994), i.e., the lower the gradient (as in the presence of 60 mM extracellular KCl), the smaller the efflux of K^+ through the open channels, along with its reversal by the selective $K_{Ca}1.1$ channel blocker iberiotoxin, suggested that the contribution of $K_{Ca}1.1$ channel stimulation by the flavonoid has functional implications for vessel mechanics. The observation that neither iberiotoxin nor glibenclamide fully reversed the antispasmodic activity of the flavonoid and pinacidil, respectively, adds further support to the notion of a significant vasodilatory mechanism independent of the stimulation of K^+ channels for both compounds (this paper; Lebrun et al., 1990). This once again underscores the bi-functional vasorelaxant effect of 3,3′-*O*-dimethylquercetin.

Due to the inherent limitations in data collected from *in vitro* experiments, further *in vivo* investigations are now necessary to determine whether the current findings contribute to the growing body of evidence supporting Brazilian green propolis as a versatile remedy for various conditions, including inflammation (Dos Santos et al., 2022), hypertension (Batista et al., 2020; Silva et al., 2021), immune-related diseases (de Figueiredo et al., 2014), and oral cavity issues (Carvalho et al., 2019).

In conclusion, the results obtained from electrophysiological, functional, and *in silico* analyses: 1) offer the first direct experimental proof that 3,3′-*O*-dimethylquercetin acts as a dual-function vasorelaxant agent, blocking $Ca_V1.2$ channels and stimulating $K_{Ca}1.1$ channels; 2) introduce a new element to the vasoactive capabilities of propolis (Beserra et al., 2020); 3) and likely provide a mechanistic explanation for previous studies conducted on vascular preparations (e.g., Massaro et al., 2013).

Ethics statement

All procedures were in strict accordance with the European Union Guidelines for the Care and the Use of Laboratory Animals (European Union Directive, 2010/63/EU) and approved by the Animal Care and Ethics Committee of the University of Siena and the Italian Department of Health (7DF19.N.TBT).

Funding

This work was supported by the FAPESP Foundation (grant number #2017/04138-8 and fellowships #2021/01411-0 and #2017/08386-6).

CRediT authorship contribution statement

Ninh The Son: Writing – review & editing, Writing – original draft, Investigation, Formal analysis, Data curation. **Beatrice Gianibbi:** Investigation, Formal analysis, Data curation. **Alice Panti:** Investigation, Formal analysis, Data curation. **Ottavia Spiga:** Writing – review & editing, Writing – original draft, Supervision, Investigation, Conceptualization. **Jairo Kenupp Bastos:** Writing – review & editing, Supervision, Conceptualization. **Fabio Fusi:** Writing – review & editing, Writing – original draft, Supervision, Investigation, Formal analysis, Data curation, Conceptualization.

Declaration of competing interest

The authors declare no competing financial interest.

Data availability

Data will be made available on request.

Acknowledgements

We express our gratitude to Dr. M. Cicogni, V. Bachini, and C. Chirillo for their valuable assistance in conducting some preliminary experiments. Special thanks to Dr. P. Fiorenzani for providing technical support. Additionally, we extend our appreciation to H. Breyer (Breyer Company, Paraná, Brazil) for aiding in the collection of plant and propolis samples in Remanso, Bahia, Brazil.

Appendix A. Supplementary data

Supplementary data to this article can be found online at https://doi.org/10.1016/j.ejphar.2024.176400.

References

Ahmed, A., Trezza, A., Gentile, M., Paccagnini, E., Panti, A., Lupetti, P., Spiga, O., Bova, S., Fusi, F., 2023. Dynamin-independent $Ca_V1.2$ and $K_{Ca}1.1$ channels regulation and vascular tone modulation by the mitochondrial fission inhibitors dynasore and dyngo-4a. Eur. J. Pharmacol. 951, 175786 https://doi.org/10.1016/j.ejphar.2023.175786.

Alday, E., Valencia, D., Garibay-Escobar, A., Domínguez-Esquivel, Z., Piccinelli, A.L., Rastrelli, L., Monribot-Villanueva, J., Guerrero-Analco, J.A., Robles-Zepeda, R.E., Hernandez, J., Velazquez, C., 2019. Plant origin authentication of *Sonoran Desert* propolis: an antiproliferative propolis from a semi-arid region. Naturwissenschaften 106 (5–6), 25. https://doi.org/10.1007/s00114-019-1620-2.

Altabbal, S., Athamnah, K., Rahma, A., Wali, A.F., Eid, A.H., Iratni, R., Al Dhaheri, Y., 2023. Propolis: a detailed insight of its anticancer molecular mechanisms. Pharmaceuticals 16 (3), 450. https://doi.org/10.3390/ph16030450.

Batista, M.A.C., Braga, D.C.A., de Moura, S.A.L., de Souza, G.H.B., Dos Santos, O.D.H., Cardoso, L.M., 2020. Salt-dependent hypertension and inflammation: targeting the gut-brain axis and the immune system with Brazilian green propolis. Inflammopharmacology 28 (5), 1163–1182. https://doi.org/10.1007/s10787-020-00742-2.

Bauer, P., Hess, B., Lindahl, E., 2023. GROMACS 2022.5 manual. Zenodo. https://doi.org/10.5281/zenodo.7586765 (2022.5).

Bean, B.P., 1984. Nitrendipine block of cardiac calcium channels: high-affinity binding to the inactivated state. Proc. Natl. Acad. Sci. U.S.A. 81 (20), 6388–6392. https://doi.org/10.1073/pnas.81.20.6388.

Beserra, F.P., Gushiken, L.F.S., Hussni, M.F., Ribeiro, V.P., Bonamin, F., Jackson, C.J., Pellizzon, C.H., Bastos, J.K., 2020. Artepillin C as an outstanding phenolic compound of Brazilian green propolis for disease treatment: a review on pharmacological aspects. Phytother Res. https://doi.org/10.1002/ptr.6875 (in press).

Bova, S., Trevisi, L., Debetto, P., Cima, L., Furnari, M., Luciani, S., Padrini, R., Cargnelli, G., 1996. Vasorelaxant properties of norbormide, a selective vasoconstrictor agent for the rat microvasculature. Br. J. Pharmacol. 117 (6), 1041–1046. https://doi.org/10.1111/j.1476-5381.1996.tb16694.x.

Carullo, G., Ahmed, A., Trezza, A., Spiga, O., Brizzi, A., Saponara, S., Fusi, F., Aiello, F., 2020. Design, synthesis and pharmacological evaluation of ester-based quercetin derivatives as selective vascular $K_{Ca}1.1$ channel stimulators. Bioorg. Chem. 105, 104404 https://doi.org/10.1016/j.bioorg.2020.104404.

Carullo, G., Saponara, S., Ahmed, A., Gorelli, B., Mazzotta, S., Trezza, A., Gianibbi, B., Campiani, G., Fusi, F., Aiello, F., 2022. Novel labdane diterpenes-based synthetic derivatives: identification of a bifunctional vasodilator that inhibits $Ca_V1.2$ and stimulates $K_{Ca}1.1$ channels. Mar. Drugs 20 (8), 515. https://doi.org/10.3390/md20080515.

Carvalho, C., Fernandes, W.H.C., Mouttinho, T.B.F., Souza, D.M., Marcucci, M.C., D'Alpino, P.H.P., 2019. Evidence-based studies and perspectives of the use of brazilian green and red propolis in dentistry. Eur. J. Dermatol. 13 (3), 459–465. https://doi.org/10.1055/s-0039-1700598.

Chavda, V.P., Chaudhari, A.Z., Teli, D., Balar, P., Vora, L., 2023. Propolis and their active constituents for chronic diseases. Biomedicines 11 (2), 259. https://doi.org/10.3390/biomedicines11020259.

Cunha, G.A.D., Carlstrom, P.F., Franchin, M., Alencar, S.M., Ikegaki, M., Rosalen, P.L., 2023. A systematic review of the potential effects of propolis extracts on experimentally-induced diabetes. Planta Med. 89 (3), 236–244. https://doi.org/10.1055/a-1910-3505.

Cuong, N.M., Son, N.T., Nhan, N.T., Khanh, P.N., Huong, T.T., Tram, N.T.T., Sgaragli, G., Ahmed, A., Trezza, A., Spiga, O., Fusi, F., 2020. Vasorelaxing activity of *R*-(-)-3'-hydroxy-2,4,5-trimethoxydalbergiquinol from *Dalbergia tonkinensis*: involvement of smooth muscle $Ca_V1.2$ channels. Planta Med. 86 (4), 284–293. https://doi.org/10.1055/a-1099-2929.

de Almeida-Junior, S., Ferraz, M.V.F., de Oliveira, A.R., Maniglia, F.P., Bastos, J.K., Furtado, R.A., 2023. Advances in the phytochemical screening and biological potential of propolis. Fundam. Clin. Pharmacol. https://doi.org/10.1111/fcp.12898, 10.1111/fcp.12898.

de Figueiredo, S.M., Nogueira-Machado, J.A., Almeida Bde, M., Abreu, S.R., de Abreu, J. A., Filho, S.A., Binda, N.S., Caligiorne, R.B., 2014. Immunomodulatory properties of green propolis. Recent Pat. Endocr. Metab. Immune Drug Discov. 8 (2), 85–94. https://doi.org/10.2174/1872214808666140619115319.

Dos Santos, F.F., Morais-Urano, R.P., Cunha, W.R., de Almeida, S.G., Cavallari, P.S.D.S. R., Manuquian, H.A., Pereira, H.A., Furtado, R., Santos, M.F.C., Amdrade E Silva, M. L., 2022. A review on the anti-inflammatory activities of Brazilian green, brown and red propolis. J. Food Biochem. 46 (10), e14350 https://doi.org/10.1111/jfbc.14350.

Fabiato, A., Fabiato, F., 1979. Calculator programs for computing the composition of the solutions containing multiple metals and ligands used for experiments in skinned muscle cells. J. Physiol. (Paris) 75 (5), 463–505.

Faul, F., Erdfelder, E., Lang, A.G., Buchner, A., 2007. G*Power 3: a flexible statistical power analysis program for the social, behavioral, and biomedical sciences. Behav. Res. Methods 39 (2), 175–191. https://doi.org/10.3758/bf03193146.

Fransen, P., Van Hove, C.E., van Langen, J., Schrijvers, D.M., Martinet, W., De Meyer, G. R., Bult, H., 2012. Contribution of transient and sustained calcium influx, and sensitization to depolarization-induced contractions of the intact mouse aorta. BMC Physiol. 12, 9. https://doi.org/10.1186/1472-6793-12-9.

Friesner, R.A., Banks, J.L., Murphy, R.B., Halgren, T.A., Klicic, J.J., Mainz, D.T., Repasky, M.P., Knoll, E.H., Shelley, M., Perry, J.K., Shaw, D.E., Francis, P., Shenkin, P.S., 2004. Glide: a new approach for rapid, accurate docking and scoring. 1. Method and assessment of docking accuracy. J. Med. Chem. 47 (7), 1739–1749. https://doi.org/10.1021/jm0306430.

Friesner, R.A., Murphy, R.B., Repasky, M.P., Frye, L.L., Greenwood, J.R., Halgren, T.A., Sanschagrin, P.C., Mainz, D.T., 2006. Extra precision glide: docking and scoring incorporating a model of hydrophobic enclosure for protein-ligand complexes. J. Med. Chem. 49 (21), 6177–6196. https://doi.org/10.1021/jm0512560.

Fusi, F., Manetti, F., Durante, M., Sgaragli, G., Saponara, S., 2016. The vasodilator papaverine stimulates L-type Ca(2+) current in rat tail artery myocytes via a PKA-dependent mechanism. Vasc. Pharmacol. 76, 53–61. https://doi.org/10.1016/j.vph.2015.11.041.

Fusi, F., Spiga, O., Trezza, A., Sgaragli, G., Saponara, S., 2017. The surge of flavonoids as novel, fine regulators of cardiovascular Ca_V channels. Eur. J. Pharmacol. 796, 158–174. https://doi.org/10.1016/j.ejphar.2016.12.033.

Fusi, F., Trezza, A., Tramaglino, M., Sgaragli, G., Saponara, S., Spiga, O., 2020. The beneficial health effects of flavonoids on the cardiovascular system: focus on K^+ channels. Pharmacol. Res. 152, 104625 https://doi.org/10.1016/j.phrs.2019.104625.

Gessner, G., Cui, Y.M., Otani, Y., Ohwada, T., Soom, M., Hoshi, T., Heinemann, S.H., 2012. Molecular mechanism of pharmacological activation of BK channels. Proc. Natl. Acad. Sci. U.S.A. 109 (9), 3552–3557. https://doi.org/10.1073/pnas.1114321109.

Greenwood, J.R., Calkins, D., Sullivan, A.P., Shelley, J.C., 2010. Towards the comprehensive, rapid, and accurate prediction of the favorable tautomeric states of drug-like molecules in aqueous solution. J. Comput. Aided Mol. Des. 24 (6–7), 591–604. https://doi.org/10.1007/s10822-010-9349-1.

Gurney, A.M., 1994. Mechanisms of drug-induced vasodilation. J. Pharm. Pharmacol. 46 (4), 242–251. https://doi.org/10.1111/j.2042-7158.1994.tb03789.x.

Halgren, T.A., Murphy, R.B., Friesner, R.A., Beard, H.S., Frye, L.L., Pollard, W.T., Banks, J.L., 2004. Glide: a new approach for rapid, accurate docking and scoring. 2. Enrichment factors in database screening. J. Med. Chem. 47 (7), 1750–1759. https://doi.org/10.1021/jm030644s.

Hossain, S., Yousaf, M., Liu, Y., Chang, D., Zhou, X., 2022. An overview of the evidence and mechanism of drug-herb interactions between propolis and pharmaceutical drugs. Front. Pharmacol. 13, 876183 https://doi.org/10.3389/fphar.2022.876183.

Huang, S., Zhang, C.P., Wang, K., Li, G.Q., Hu, F.L., 2014. Recent advances in the chemical composition of propolis. Molecules 19 (12), 19610–19632. https://doi.org/10.3390/molecules191219610.

Huang, J., Rauscher, S., Nawrocki, G., Ran, T., Feig, M., de Groot, B.L., Grubmüller, H., MacKerell Jr., A.D., 2017. CHARMM36m: an improved force field for folded and intrinsically disordered proteins. Nat. Methods 14 (1), 71–73. https://doi.org/10.1038/nmeth.4067.

Iozzi, D., Schubert, R., Kalenchuk, V.U., Neri, A., Sgaragli, G., Fusi, F., Saponara, S., 2013. Quercetin relaxes rat tail main artery partly via a PKG-mediated stimulation of $K_{Ca}1.1$ channels. Acta Physiol. 208 (4), 329–339. https://doi.org/10.1111/apha.12083.

Karmažínová, M., Lacinová, L., 2010. Measurement of cellular excitability by whole cell patch clamp technique. Physiol. Res. 59 (Suppl. 1), S1–S7. https://doi.org/10.33549/physiolres.932000.

Kim, S., Chen, J., Cheng, T., Gindulyte, A., He, J., He, S., Li, Q., Shoemaker, B.A., Thiessen, P.A., Yu, B., Zaslavsky, L., Zhang, J., Bolton, E.E., 2023. PubChem 2023 update. Nucleic Acids Res. 51 (D1), D1373–D1380. https://doi.org/10.1093/nar/gkac956.

Kubota, Y., Umegaki, K., Kobayashi, K., Tanaka, N., Kagota, S., Nakamura, K., Kunitomo, M., Shinozuka, K., 2004. Anti-hypertensive effects of Brazilian propolis in spontaneously hypertensive rats. Clin. Exp. Pharmacol. Physiol. 31 (Suppl. 2), S29–S30. https://doi.org/10.1111/j.1440-1681.2004.04113.x.

Kuriyama, H., Kitamura, K., Nabata, H., 1995. Pharmacological and physiological significance of ion channels and factors that modulate them in vascular tissues. Pharmacol. Rev. 47 (3), 387–573.

Lebrun, P., Fang, Z.Y., Antoine, M.H., Herchuelz, A., Hermann, M., Berkenboom, G., Fontaine, J., 1990. Hypoglycemic sulfonylureas antagonize the effects of cromakalim and pinacidil on ^{86}Rb fluxes and contractile activity in the rat aorta. Pharmacology 41 (1), 36–48.

Lu, C., Wu, C., Ghoreishi, D., Chen, W., Wang, L., Damm, W., Ross, G.A., Dahlgren, M.K., Russell, E., Von Bargen, C.D., Abel, R., Friesner, R.A., Harder, E.D., 2021. OPLS4: improving force field accuracy on challenging regimes of chemical space. J. Chem. Theor. Comput. 17 (7), 4291–4300. https://doi.org/10.1021/acs.jctc.1c00302.

Magnon, M., Calderone, V., Floch, A., Cavero, I., 1998. Influence of depolarization on vasorelaxant potency and efficacy of Ca^{2+} entry blockers, K^+ channel openers,

nitrate derivatives, salbutamol and papaverine in rat aortic rings. Naunyn-Schmiedeberg's Arch. Pharmacol. 358 (4), 452–463. https://doi.org/10.1007/pl00005278.

Maruyama, H., Sumitou, Y., Sakamoto, T., Araki, Y., Hara, H., 2009. Antihypertensive effects of flavonoids isolated from brazilian green propolis in spontaneously hypertensive rats. Biol. Pharm. Bull. 32 (7), 1244–1250. https://doi.org/10.1248/bpb.32.1244.

Massaro, F.C., Brooks, P.R., Wallace, H.M., Nsengiyumva, V., Narokai, L., Russell, F.D., 2013. Effect of Australian propolis from stingless bees (*Tetragonula carbonaria*) on pre-contracted human and porcine isolated arteries. PLoS One 8 (11), e81297. https://doi.org/10.1371/journal.pone.0081297.

McDonald, T.F., Pelzer, S., Trautwein, W., Pelzer, D.J., 1994. Regulation and modulation of calcium channels in cardiac, skeletal, and smooth muscle cells. Physiol. Rev. 74 (2), 365–507. https://doi.org/10.1152/physrev.1994.74.2.365.

Mendonça, L., Frota, V.M., Pinto, B.J.F., dos Santos Moita, E.C., da Hora, J.P., Costa, M. F., Fernandes, J.A.B., Zocolo, G.J., Gomes, G.A., do Vale, J.P.C., Bandeira, P.N., dos Santos, H.S., Rodrigues, T.H.S., 2021. Seasonality in the volatile oil composition of green propolis from the Caatinga biome. Rev. Bras. Farmacogn. 31, 497–501. https://doi.org/10.1007/s43450-021-00186-x.

Mugnai, P., Durante, M., Sgaragli, G., Saponara, S., Paliuri, G., Bova, S., Fusi, F., 2014. L-type Ca(2+) channel current characteristics are preserved in rat tail artery myocytes after one-day storage. Acta Physiol. 211 (2), 334–345. https://doi.org/10.1111/apha.12282.

Nazari-Bonab, H., Jamilian, P., Radkhah, N., Zarezadeh, M., Ebrahimi-Mameghani, M., 2023. The effect of propolis supplementation in improving antioxidant status: a systematic review and meta-analysis of controlled clinical trials. Phytother Res. https://doi.org/10.1002/ptr.7899, 10.1002/ptr.7899.

Schrödinger Release 2022-3, 2022. LigPrep. Schrödinger, LLC, New York, NY.

Saponara, S., Sgaragli, G., Fusi, F., 2002. Quercetin as a novel activator of L-type Ca(2+) channels in rat tail artery smooth muscle cells. Br. J. Pharmacol. 135 (7), 1819–1827. https://doi.org/10.1038/sj.bjp.0704631.

Saponara, S., Testai, L., Iozzi, D., Martinotti, E., Martelli, A., Chericoni, S., Sgaragli, G., Fusi, F., Calderone, V., 2006. (+/-)-Naringenin as large conductance Ca(2+)-activated K^+ (BK_{Ca}) channel opener in vascular smooth muscle cells. Br. J. Pharmacol. 149 (8), 1013–1021. https://doi.org/10.1038/sj.bjp.0706951.

Segueni, N., Boutaghane, N., Asma, S.T., Tas, N., Acaroz, U., Arslan-Acaroz, D., Shah, S. R.A., Abdellatieff, H.A., Akkal, S., Peñalver, R., Nieto, G., 2023. Review on propolis applications in food preservation and active packaging. Plants 12 (8), 1654. https://doi.org/10.3390/plants12081654.

Shelley, J.C., Cholleti, A., Frye, L.L., Greenwood, J.R., Timlin, M.R., Uchimaya, M., 2007. Epik: a software program for pKa prediction and protonation state generation for drug-like molecules. J. Comput. Aided Mol. Des. 21 (12), 681–691. https://doi.org/10.1007/s10822-007-9133-z.

Silva, H., Francisco, R., Saraiva, A., Francisco, S., Carrascosa, C., Raposo, A., 2021. The cardiovascular therapeutic potential of propolis-a comprehensive review. Biology 10 (1), 27. https://doi.org/10.3390/biology10010027.

Simplicio, J.A., Pernomian, L., Simão, M.R., Carnio, E.C., Batalhão, M.E., Ambrosio, S.R., Tirapelli, C.R., 2014. Mechanisms underlying the vascular and hypotensive actions of the labdane ent-3-acetoxy-labda-8(17),13-dien-15-oic acid. Eur. J. Pharmacol. 726, 66–76. https://doi.org/10.1016/j.ejphar.2014.01.018.

Son, N.T., Ribeiro, V.P., Bastos, J.K., 2022. Flavonoids from green propolis of the Northeastern Brazilian caatinga *Mimosa tenuiflora* (Wild.) Poir: a chemotaxonomic aspect. Biochem. Systemat. Ecol. 104, 104473 https://doi.org/10.1016/j.bse.2022.104473.

Tao, X., MacKinnon, R., 2019. Molecular structures of the human Slo1 K^+ channel in complex with β4. Elife 8, e51409. https://doi.org/10.7554/eLife.51409.

Teixeira, E.W., Negri, G., Meira, R.M., Message, D., Salatino, A., 2005. Plant origin of green propolis: bee behavior, plant anatomy and chemistry. Evid. Based Complement. Alternat. Med. 2 (1), 85–92. https://doi.org/10.1093/ecam/neh055.

Trezza, A., Spiga, O., Mugnai, P., Saponara, S., Sgaragli, G., Fusi, F., 2022. Functional, electrophysiology, and molecular dynamics analysis of quercetin-induced contraction of rat vascular musculature. Eur. J. Pharmacol. 918, 174778 https://doi.org/10.1016/j.ejphar.2022.174778.

Tykocki, N.R., Boerman, E.M., Jackson, W.F., 2017. Smooth muscle ion channels and regulation of vascular tone in resistance arteries and arterioles. Compr. Physiol. 7 (2), 485–581. https://doi.org/10.1002/cphy.c160011.

Uniprot Consortium, 2023. UniProt: the universal protein knowledgebase in 2023. Nucleic Acids Res. 51 (D1), D523–D531. https://doi.org/10.1093/nar/gkac1052.

Xu, C., Tang, G., Lu, Y., Wang, R., 2000. Molecular basis of voltage-dependent delayed rectifier K^+ channels in smooth muscle cells from rat tail artery. Life Sci. 66 (21), 2023–2033. https://doi.org/10.1016/s0024-3205(00)00529-4.

Yao, L., Jiang, Y., Singanusong, R., D'Arcy, B., Datta, N., Caffin, N., Raymont, K., 2004. Flavonoids in *Australian melaleuca, guioa, lophostemon, banksia* and *helianthus* honeys and their potential for floral authentication. Food Res. Int. 37, 166–174. https://doi.org/10.1016/j.foodres.2003.11.004.

Zhao, Y., Huang, G., Wu, J., Wu, Q., Gao, S., Yan, Z., Lei, J., Yan, N., 2019. Molecular basis for ligand modulation of a mammalian voltage-gated Ca^{2+} channel. Cell 177 (6), 1495–1506. https://doi.org/10.1016/j.cell.2019.04.043 e12.

Zulhendri, F., Chandrasekaran, K., Kowacz, M., Ravalia, M., Kripal, K., Fearnley, J., Perera, C.O., 2021. Antiviral, antibacterial, antifungal, and antiparasitic properties of propolis: a review. Foods 10 (6), 1360. https://doi.org/10.3390/foods10061360.

Zulhendri, F., Lesmana, R., Tandean, S., Christoper, A., Chandrasekaran, K., Irsyam, I., Suwantika, A.A., Abdulah, R., Wathoni, N., 2022. Recent update on the anti-inflammatory activities of propolis. Molecules 27 (23), 8473. https://doi.org/10.3390/molecules27238473.

Zullkiflee, N., Taha, H., Usman, A., 2022. Propolis: its role and efficacy in human health and diseases. Molecules 27 (18), 6120. https://doi.org/10.3390/molecules27186120.